



LAWRENCE
LIVERMORE
NATIONAL
LABORATORY

Understanding reliability and limitations of the images and spectra reconstructed from a multi-monochromatic x-ray imager

T. Nagayama, R. C. Mancini, D. Mayes, R. Tommasini, R. Florido

April 8, 2016

Review of Scientific Instruments

Disclaimer

This document was prepared as an account of work sponsored by an agency of the United States government. Neither the United States government nor Lawrence Livermore National Security, LLC, nor any of their employees makes any warranty, expressed or implied, or assumes any legal liability or responsibility for the accuracy, completeness, or usefulness of any information, apparatus, product, or process disclosed, or represents that its use would not infringe privately owned rights. Reference herein to any specific commercial product, process, or service by trade name, trademark, manufacturer, or otherwise does not necessarily constitute or imply its endorsement, recommendation, or favoring by the United States government or Lawrence Livermore National Security, LLC. The views and opinions of authors expressed herein do not necessarily state or reflect those of the United States government or Lawrence Livermore National Security, LLC, and shall not be used for advertising or product endorsement purposes.

Understanding reliability and limitations of the images and spectra reconstructed from a multi-monochromatic x-ray imager

T. Nagayama,^a R. C. Mancini, and D. Mayes
Physics Department, University of Nevada, Reno, NV

R. Tommasini
Lawrence Livermore National Laboratory, Livermore, CA

R. Florido
Departamento de Física, Universidad de Las Palmas de Gran Canaria, 35017 Las Palmas de Gran Canaria, Spain
(Dated: June 5, 2015)

Temperature and density asymmetry diagnosis is critical to advance inertial confinement fusion (ICF) science. A multi-monochromatic x-ray imager (MMI) is an attractive diagnostic for this purpose. The MMI records the spectral signature from an ICF implosion core with time resolution, 2-D space-resolution, and spectral resolution. While narrow-band images and 2-D space-resolved spectra from the MMI data constrain temperature and density spatial structure of the core, the accuracy of the images and spectra highly depends on the quality of the MMI data and the post-processing tools. Here, we synthetically quantify the accuracy of images and spectra reconstructed from MMI data. The errors in the reconstructed images are less than a few percent when the space-resolution effect is applied on the modeled images. The errors in the reconstructed 2-D space-resolved spectra are also less than a few percent except those for the peripheral regions. The spectra reconstructed for the peripheral regions have slightly but systematically lower intensities by $\sim 6\%$ due to the instrumental spatial-resolution effects. However, this does not alter the relative line ratios and widths, and thus does not affect the temperature and density diagnostics. We also investigate the impact of the pinhole size variation on the extracted images and spectra. A 10% pinhole size variation could introduce spatial bias to the images and spectra of $\sim 10\%$. A correction algorithm is developed, and it successfully reduces the errors to a few percent. It is desirable to perform similar synthetic investigations to fully understand the reliability and limitations of each MMI application.

I. INTRODUCTION

Inertial confinement fusion (ICF) is a concept for an alternative energy source, which releases energy by compressing a millimeter-scale capsule containing fusion fuel (i.e., hydrogen isotopes such as tritium, T, and deuterium, D) with ablation pressure driven by mega-joule lasers [1, 2]. Substantial progress has been made in theory, experiment, and diagnostics of ICF. However, efficient fuel burn, or *ignition*, has not yet been achieved, and discrepancies between experiments and simulations still remain [3]. While sources of discrepancies are extensively investigated [4], diagnostics that directly reveal the evolution of the ICF implosion-plasma spatial structure are desired to advance ICF science towards ignition.

Multi-monochromatic x-ray imagers (MMI) are attractive instruments for this purpose. The MMI is a unique 2-D spectrometer consisting of a pinhole array, a multi-layered mirror (MLM), and microchannel plates (MCP) [5, 6]. It records an array of ICF implosion-core images, each of which is formed by photons of slightly different wavelength. By processing MMI data, one can extract narrow-band images (i.e., intensity images of a narrow spectral range), space-integrated spectra [7–9], and 2-D

space-resolved spectra [10]. Spectroscopic analysis of the MMI data provide a variety of approaches to constrain ICF plasma spatial structure in electron temperature, T_e , and electron density, n_e .

For example, we mixed a small fraction of Ar into D_2 gas fuel and analyzed Ar line emission to characterize T_e and n_e of the core. Using two narrow-band images, we inferred time-resolved 2-D T_e maps [11], and from a collection of space-resolved spectra, we extracted T_e maps as well as n_e maps [10]. Synthetic investigations also suggest that time-resolved 3-D T_e and n_e spatial structure of ICF implosion cores can be studied by simultaneously analyzing collections of 2-D space-resolved spectra extracted from three MMI instruments fielded along quasi-orthogonal lines of sight [12]. Thus, MMI diagnostics have the potential to better constrain the ICF experiments and advance ICF theory.

For reliable MMI diagnostics, the pinhole array needs to be properly tilted to optimize the spatial sampling efficiency, and the sampling width needs to be much narrower than the spectral width of the diagnostic lines [13]. When this criterion is satisfied, the images and space-resolved spectra extracted from the MMI data [9, 10] become reliable.

In this paper, we quantitatively investigate the accuracy of the reconstructed images and spectra for the application to the Ar-doped D_2 ICF implosion experiments. Specifically, we show synthetic investigations for

^a Present address: Sandia National Laboratories, Albuquerque, NM

the spatial- and spectral-resolution effects. These effects are not obvious because resolution affects the MMI data first and then are propagated to the reconstructed images and spectra through the processing discussed in Refs. [9, 10]. For example, images and spectra would be affected both by spatial resolution and spectral resolution.

We found that the reconstructed images are accurate within a few-percent error as long as a point-spread function is applied to the modeled image. The spectral-resolution effects on the image are negligible for our application because the line images are integrated over their spectral line width, which is much broader than the spectral resolution of the instrument.

Extracted space-resolved spectra are accurate within a few-percent error for the central region of the image as long as spectral-resolution effects are applied on the modeled space-resolved spectra. Spectra extracted from the periphery show an average absolute error of $\sim 6 - 7\%$. The larger discrepancies originate from the systematic intensity drop due to spatial convolution over the image boundary and from periodic artifacts due to rapid intensity drop at the periphery. Since the intensity drop is systematic and the periodic artifacts oscillate about the expected value, their effects on the line ratio and width are much smaller. The T_e and n_e inferred from those spectra are accurate within a few-percent error.

We also investigated individual pinhole size variation and its effect on the images and spectra. This can introduce artificial spatial bias of $\sim 10\%$. We developed a technique to correct the pinhole size-variation effects on the MMI data. The correction successfully removes the spatial bias and suppresses the errors to within a few percent.

The article is organized as follows. Sec. II describes the spectral model used to create synthetic MMI data and also to compute expected images and spectra. In Sec. III, we quantitatively investigate the spatial-resolution and spectral-resolution effects. Sec. IV describes pinhole size-variation effects on the extracted images and spectra, as well as their correction. Sec. V provides discussion and summary.

II. SPECTRAL MODEL

A. Emergent spectra as a function of (x, y) on the image plane

Our spectral model computes emergent spectra at every point on the image plane, $I_\nu(x, y)$, and then $I_\nu(x, y)$ is used to compute both synthetic MMI data and expected images and spectra. The case of investigation is an OMEGA direct-drive Ar-doped D_2 ICF implosion because it has been one of our main applications for the MMI diagnostic [10, 11]. Ar atomic concentration in those applications is 0.18%. Ar spectral emissivity and opacity are computed for a given T_e and n_e spatial distributions taking into account free electrons contributed

from ionized D and Ar. The emergent spectra are computed by solving the radiation transport along each chord parallel to the line of sight [12].

To compute the Ar emissivity, ϵ_ν , and opacity, κ_ν , necessary atomic data are computed by Flexible Atomic Code (FAC) [14], and Ar level populations are solved for grids of T_e and n_e with a collisional-radiative model, ABAKO[15]. We used the Stewart and Pyatt model [16] for continuum-lowering effects and the escape factor of a sphere to account for photo-pumping effects on the populations [17]. Spectral emissivity and opacity are computed from the calculated populations taking into account detailed Stark line profiles computed by MERL [18].

Emergent spectra are computed along each chord on the image plane by solving the radiation transport equation assuming parallel ray tracing [19]:

$$I_\nu(x, y) = \int_{z_{\text{rear}}}^{z_{\text{front}}} \frac{\epsilon_\nu(x, y, z)}{\kappa_\nu(x, y, z)} \left\{ 1 - e^{-\tau_\nu(x, y, z)} \right\} dz \quad (1)$$

$$\tau_\nu(x, y, z) = \int_z^{z_{\text{front}}} \kappa_\nu(x, y, z') dz' \quad (2)$$

where the z axis is parallel to the line of sight, the x - y plane is parallel to the image plane of the detector, $I_\nu(x, y)$ is the emergent intensity at (x, y) on the observer side of the source [erg/s/cm²/sr/eV], and τ_ν is the optical depth from point z to the observer side of the object surface. If (x, y, z) is inside the object, the quantities $\epsilon_\nu(x, y, z)$ and $\kappa_\nu(x, y, z)$ are determined at the given T_e and n_e using ABAKO. If (x, y, z) is outside the object, both $\epsilon_\nu(x, y, z)$ and $\kappa_\nu(x, y, z)$ equal zero.

Theoretical uncertainty in the calculated emissivity and opacity does not affect the conclusions derived from the synthetic investigations performed in this article because $I_\nu(x, y)$ are used to calculate both synthetic MMI data and expected images and spectra. What we pursue is an understanding of the discrepancies due to the processing MMI data, whose spatial- and spectral-samplings are somewhat limited.

B. Expected images and spectra

Expected narrow-band images are computed by integrating $I_\nu(x, y)$ over any given spectral range as:

$$I_{\Delta\nu}(x, y) = \int_{\Delta\nu} I_\nu(x, y) d\nu \quad (3)$$

where $\Delta\nu$ is the bandwidth of interest.

Space-resolved spectra are computed by integrating $I_\nu(x, y)$ over any given spatial region of interest:

$$I_{\nu, \Delta A} = \int_{\Delta A} I_\nu(x, y) da \quad (4)$$

where ΔA is an arbitrarily shaped area of interest.

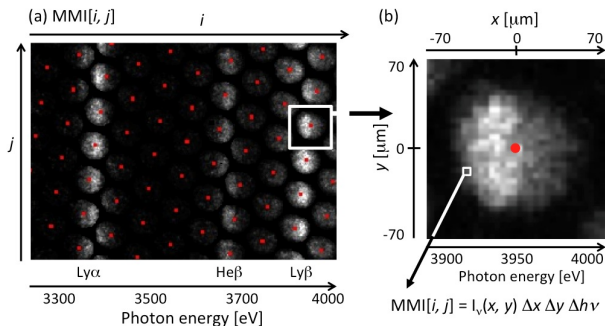


FIG. 1. (Color online) (a) MMI data after efficiency correction. i and j are the horizontal and vertical indices of the pixels, respectively. The horizontal axis is also photon energy due to the spectral dispersion by the MLM. Red dots mark the pinhole-image centers. (b) Blow-up of one pinhole image. Each image has its own local spatial coordinates of the implosion core, (x, y) . Each pixel value is proportional to $I_\nu(x, y) \Delta h\nu \Delta x \Delta y$.

There are two different ways to deal with the instrumental-resolution effects. One is to deconvolve the resolution effects from the data. The other is to convolve resolution effects into the modeled images and spectra. We use the latter option because it is more straightforward. For example, we can apply a 2-D Gaussian point-spread function to the expected images to account for instrumental spatial-resolution effects. Also, a 1-D Gaussian spectral profile can be applied to the expected spectra that account for instrumental spectral-resolution effects on the spectra.

C. Synthetic MMI data

FIG. 1 (a) shows example MMI data. The detector plane is packed with a hexagonal array of pinhole implosion-core images. Due to the reflection of the MLM, each column of the MMI data pick out the signals of specific photon energy, and the horizontal axis is also in photon energy units. FIG. 1 (b) is a blow-up of one pinhole image. After correcting for magnification, each pinhole image has its own local spatial coordinate of the implosion core, (x, y) .

Thus, each pixel of the MMI data, $\text{MMI}[i, j]$, represents signals at a local position of the implosion core surface, $(x \pm \Delta x/2, y \pm \Delta y/2)$, of a very small spectral range, $h\nu \pm \Delta h\nu/2$. To model MMI data, the value of each pixel, $\text{MMI}[i, j]$, is computed as $I_\nu(x, y) \Delta h\nu \Delta x \Delta y$ where $\Delta h\nu$ and $\Delta x \Delta y$ are the spectral and spatial width of the pixel, $[i, j]$ (i.e., not the resolution of the instrument). The mapping from the MMI pixel $[i, j]$ to the corresponding point in the object space, (x, y) , and the corresponding photon energy, $h\nu$, are different for every dataset and determined through the processing described in Ref. [9]. Synthetic investigation becomes more useful when the mapping information comes from the actual

data of interest.

Then, the spatial- and spectral-resolution effects are applied on the synthetic MMI data. Spatial resolution due to the pinholes are applied by convolving a 2-D Gaussian point-spread function of a given spatial resolution. Spectral-resolution effects are applied by convolving the synthetic MMI data with a Gaussian profile of a given resolution power along horizontal direction.

The model also has an option to simulate pinhole size-variation effects due to an individual pinhole tolerance. For a given nominal pinhole size and its tolerance, it uses a Gaussian random number generator to assign a slightly different pinhole size to each pinhole. Slight differences in spatial resolution and brightness are simulated for each pinhole image based on the assigned pinhole size. These options for spatial resolution, spectral resolution, and pinhole-size variation are useful to investigate their effects on the reconstructed images and spectra.

III. QUANTITATIVE INVESTIGATIONS OF SPATIAL AND SPECTRAL RESOLUTION EFFECTS

The accuracy of the narrow-band images and spectra reconstructed from MMI data are quantitatively investigated using synthetic MMI data. We create synthetic MMI data that satisfy the criterion discussed in Ref. [13]. We assume a 100- μm -diameter spherical plasma of uniform conditions ($T_e=1500$ eV and $n_e = 1.5 \times 10^{24} \text{ cm}^{-3}$). These values are characteristic values for an OMEGA direct-drive Ar-doped ICF implosion experiments reported previously [10, 11]. The pinhole-array design and photon-energy axis used for the synthetic MMI data are those from the data shown in Ref. [11] that satisfy the criterion.

Then, we apply two different levels of instrumental details as discussed in Sec. II C. The first case denoted as “ ΔE ”, takes into account spectral resolving power of $E/\Delta E=150$. The second case denoted as “ $\Delta E, \Delta x$ ”, takes into account not only spectral resolution, but also the spatial resolution of $\Delta x = 11 \mu\text{m}$. These are typical values of the spectral resolution and spatial resolution for the MLM and the pinhole arrays used in our applications.

The images and spectra are reconstructed from these synthetic MMI data [9, 10] and compared with the expected images and spectra computed as in Sec. II B. Comparisons of the images and spectra are discussed in Sec. III A and in Sec. III B, respectively.

A. Accuracy of extracted images

FIG. 2 compares Ar He- β images reconstructed from the synthetic MMI data for cases (a) “ ΔE ” and (b) “ $\Delta E, \Delta x$ ” with (c) the expected He- β . The reconstructed images for both cases agree with the expected image quite well. However, they show small artificial structures along

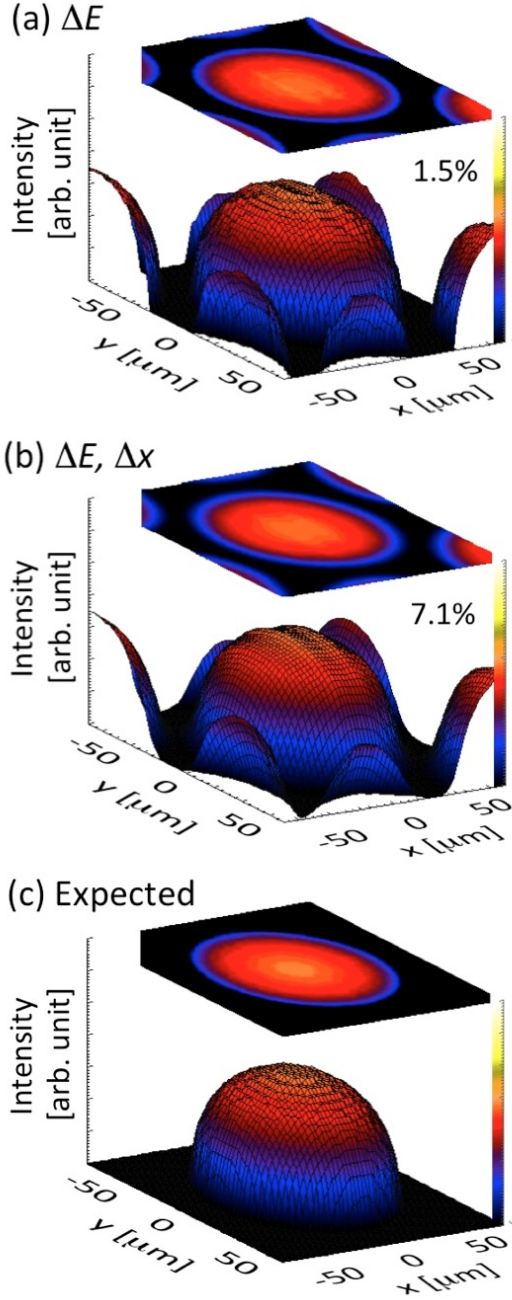


FIG. 2. (Color online) Ar He- β images reconstructed from the synthetic MMI data with (a) spectral resolution ($E/\Delta E=150$), (b) both spectral and spatial resolution ($\Delta x=11\ \mu\text{m}$). (c) Expected image computed directly from the spectral model.

the y direction, which correspond to the vertical direction on the MMI image and originate from the discrete nature of MMI data. These artifacts of a few percent in value are unavoidable and are limitations of the current MMI data and its processing technique.

The reconstructed image from the MMI data without spatial-resolution effects [FIG. 2(a)] best agrees with the

expected images with the average absolute percent error of 1.5%. When the spatial-resolution effects are applied on the synthetic MMI data, the average absolute error increases to 7.1%.

FIG. 3 (a) and (b) show percent-error surface plots computed for “ ΔE ” and “ $\Delta E, \Delta x$ ” with respect to the expected image [i.e., 2(c)]. While FIG. 3 (a) reveals that the main source of the error is from the observed vertical artifacts, the errors in (b) are largest at the image periphery. These large errors on the periphery are produced because the target image shown 2(c) do not take into account spatial-resolution effects.

Next, we apply the 2-D Gaussian point-spread function of FWHM= $11\ \mu\text{m}$ directly to the expected image and recompute the error images for the case of “ $\Delta E, \Delta x$ ” to see if such an image is a more appropriate representation of the reconstructed images. We note that this treatment does not necessarily compensate for the spatial-resolution effects on the reconstructed images. This is because they are produced by applying the point-spread function and spectral-resolution effects directly on the MMI data, and then the effects are propagated through the processing. FIG. 3 (c) shows the resultant percent-error image. The deep negative errors at the periphery disappear, and the percent error is dominated by the vertical artifacts as in the case of FIG. 3 (a). The percent error is reduced from 7.1% to 1.4%.

To summarize, the image reconstruction is reliable with the error of a few percent as long as the spatial-resolution effects are taken into account on the expected image. On one hand, the spectral-resolution effects on the reconstructed image are negligible for the applications presented here because the narrow-band images are computed by integrating a monochromatic image over its spectral line width (i.e., $\Delta E \sim 60\ \text{eV}$) as in Eq. (3), which is significantly broader than the spectral resolution of the instruments. On the other hand, the spatial-resolution effects are not negligible and mostly affect the image periphery. The intensities at the image periphery are lowered because the convolving area partially exceeds the object boundary. Small vertical errors observed in FIG. 3 (a) and (c) originate from the subtle vertical artifacts observed in FIG. 3, which are produced by the discrete nature of the MMI data.

B. Accuracy of extracted spectra

Space-resolved spectra are reconstructed from the synthetic MMI data with the technique discussed in Ref. [10]. Spatial regions defined for the space-resolved spectra are shown in FIG. 4 (a). Each spatial region can be categorized as belonging to the (b) central region, (c) top/bottom periphery, and (d) left/right periphery as shown in FIG. 4. These categories are important for understanding different sources of errors in MMI spectra. From the particular synthetic MMI data, 53 spatial regions are automatically defined using a minimum binning

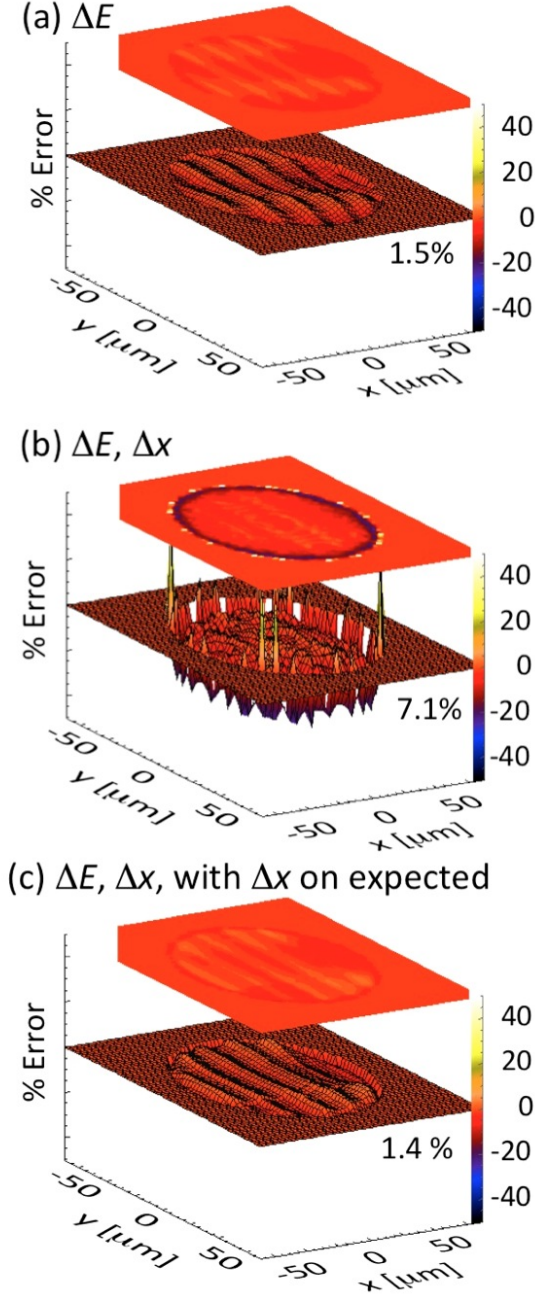


FIG. 3. (Color online) Percent-error surface plots for He- β reconstructed from the synthetic MMI data (a) with spectral resolution only and (b) with both spectral and spatial resolution. The given percentages are the average of the absolute percent errors within the image regions. (c) is the same as (b) except that spatial-resolution effects are directly applied to the expected image used in the percent-error calculation.

width comparable to the spatial resolution, $\sim 11\mu\text{m}$. In this section, one spectrum is selected from each category (i.e., regions 30, 3, and 26, respectively) to discuss the source of error, and the rest are discussed through the average percent errors for central and peripheral regions.

FIG. 5(a) compares the reconstructed space-resolved

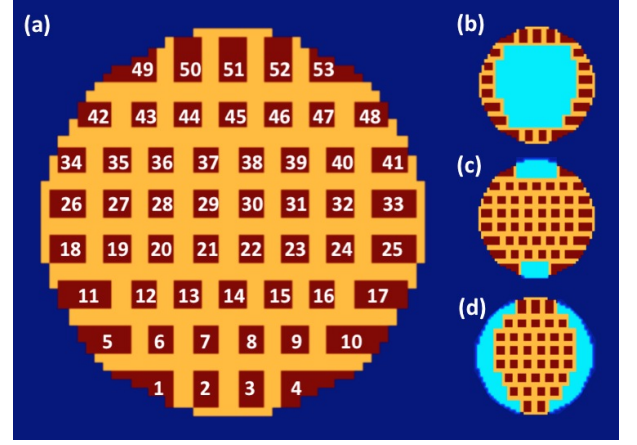


FIG. 4. (Color online) (a) rectangular spatial regions defined with spatial resolution, $\Delta x \sim 11\mu\text{m}$. (b), (c), and (d) define the central region, top/bottom periphery, and left/right periphery, respectively, which have slightly different sources of discrepancies.

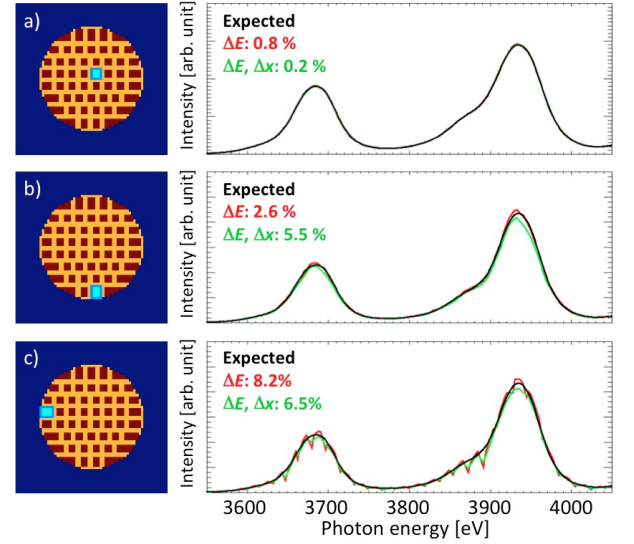


FIG. 5. (Color online) 2-D space-resolved spectra extracted from the synthetic MMI with (red) spectral-resolution effects only, (green) both spectral and spatial resolution for (a) the central region, (b) the bottom periphery, and (c) the left periphery. The percentages shown are the average absolute percent errors with respect to the expected space-resolved spectra (black).

spectra and the expected spectra for a central region [i.e., region 30 of FIG. 4(a)]. The red and green are those reconstructed from synthetic MMI computed with “ ΔE ” and “ $\Delta E, \Delta x$ ” resolution options, respectively. The green and red spectra agree very well with the expected spectrum (black) and are in fact hidden underneath the black spectrum. The average percent errors for “ ΔE ” and “ $\Delta E, \Delta x$ ” are 0.8% and 0.2%, respectively.

FIG. 5(b) shows similar comparisons for space-resolved spectra at a top/bottom-periphery region (i.e., region 3

of FIG. 4). While they still show reasonable agreement to the expected spectrum, the average percent errors increase to 2.6% and 5.5%, respectively. The increase in the percent error is mostly due to the non-negligible intensity gradient within the region. Spatial areas are defined such that the region size becomes comparable to the spatial resolution so that the intensity variation over the region becomes negligible. However, image intensity always drops rapidly towards the image periphery, and negligible variations cannot be assumed for the peripheral regions. Thus, comparison between expected and reconstructed spectra from the peripheral regions are in general not as good as those for central regions.

Spectra extracted from the periphery have other issues when finite spatial resolution is taken into account (green). Finite spatial resolution smooths out the structure, and some signals are mixed in from the adjacent regions. Thus, at the periphery, spatial-resolution effects lower the overall intensity very slightly, but systematically, because the convolving area partially exceeds the object boundary. Since the spectral-resolution size is $\sim 11 \mu\text{m}$ and small compared to the object size, these effects are subtle but still persist as observed in FIG. 3(b). In the case of image comparison, the systematic intensity drop at the periphery disappears by applying the point-spread function directly to the expected images. However, it is not as easy to take into account spatial-resolution effects in the space-resolved spectra modeling. Here, we do not introduce any correction associated with the edge effects but just summarize what we learn from the comparisons. Fortunately, their effects are small and systematic over the entire spectral range. This preserves the line ratios and widths, and thus these effects on the T_e and n_e analysis can be considered negligible.

FIG. 5(c) shows the comparisons of space-resolved spectra extracted from a left/right-periphery region (i.e., region 26) and its expected spectrum. One can observe that all the extracted space-resolved spectra show periodic structure about the expected spectrum, which results in decreasing the percent errors to 8.2% and 6.5%, respectively. This periodic structure is observed from all space-resolved spectra extracted from the left/right-periphery regions.

These periodic structures originate from the non-negligible horizontal intensity gradient in the spatial region. For left/right-periphery regions, the intrinsic radial intensity gradients become horizontal, which is a problem because the horizontal axis is also the spectral axis. FIG. 6 (a) and (b) show a blow-up of the partial MMI data associated with region 26 over the Ly- β region and the extracted spectrum, respectively. Each spatial region of FIG. 6(a) is slightly enlarged, and outside of region 26 is whitened out for communication purposes. Every region 26 on the synthetic MMI data shows horizontal intensity gradients monotonically increasing from left to right. Since each partial image is responsible for a different sub-range of the spectrum, the extracted spectrum inherits the periodic horizontal gradient structure. While we ap-

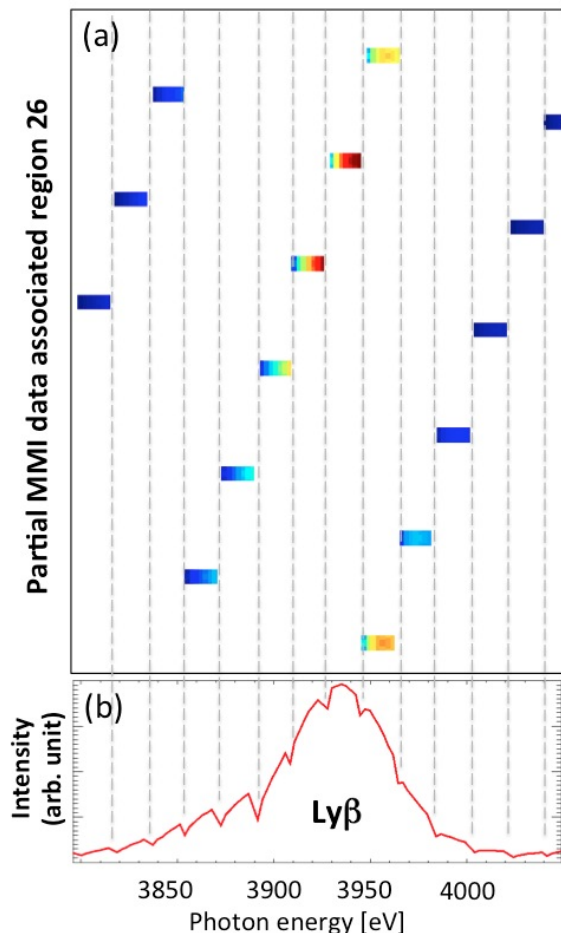


FIG. 6. (Color online) (a) A left-periphery region (region 26) is picked out from each pinhole image of the MMI data and shown over the spectral range of Ly- β . (b) The spectra extracted from the partial MMI data show periodic structure originating from the repeating horizontal intensity gradient structures of the each rectangular region. The selected regions are slightly enlarged for display purposes.

ply a first-order correction to this using the technique discussed in Sec. V of Ref. [9], the periodic structure is not perfectly removed.

Table I shows average percent errors computed for space-resolved spectra over each category defined in FIG. 4(b), (c), and (d). For the 32 central regions, extracted spectra are very accurate and show average percent error of less than 1%. Spectra extracted from the top/bottom periphery show larger discrepancies of 1.4% and 3.8%, respectively. The 1.4% is due to the non-negligible vertical intensity gradient. When the spatial-resolution effect is introduced, it slightly but systematically lowers the intensity, which results in increasing the percent error to 3.8%. For the left/right periphery, the percent errors become even larger – 5.1% and 7.5%, respectively – due to the periodic structure originating from horizontal intensity gradients.

Table II shows the percent errors in inferred T_e and

Intensity % error	ΔE	$\Delta E, \Delta x$
Central (32)	$0.6 \pm 0.3 \%$	$0.7 \pm 0.4 \%$
Top/bottom periphery (5)	$1.4 \pm 0.3 \%$	$3.8 \pm 0.3 \%$
Left/right periphery (16)	$5.1 \pm 1.2 \%$	$7.5 \pm 1.9 \%$

TABLE I. The percent errors averaged over the central, top/bottom-periphery, and left/right-periphery regions, respectively. The numbers of spectra are shown in parentheses. For peripheral regions, the percent error becomes larger when spatial-resolution effects are introduced. Left/right peripheral regions have larger errors than top/bottom peripheral region due to periodic structure introduced by the horizontal intensity gradients.

T_e % error	ΔE	$\Delta E, \Delta x$
Central (32)	$0.0 \pm 0.0\%$	$0.1 \pm 0.1\%$
Top/bottom periphery (5)	$0.4 \pm 0.5\%$	$0.5 \pm 0.6\%$
Left/right periphery (16)	$0.7 \pm 0.6\%$	$0.8 \pm 0.7\%$
n_e % error	ΔE	$\Delta E, \Delta x$
Central (32)	$0.2 \pm 0.2\%$	$0.3 \pm 0.3\%$
Top/bottom periphery (5)	$2.3 \pm 1.1\%$	$3.1 \pm 1.2\%$
Left/right periphery (16)	$1.8 \pm 2.6\%$	$1.9 \pm 2.1\%$

TABLE II. The percent errors in T_e and n_e averaged over the central, top/bottom-periphery, and left/right-periphery regions, respectively. The errors are within a few percent.

n_e and their standard deviations. Since we have both expected spectra and reconstructed spectra, we can investigate how inaccuracy introduced in the reconstructed spectra affect the inferred T_e and n_e . First, T_e and n_e are inferred from both expected spectra and reconstructed in the same way as described in Ref. [10]. The percent errors in inferred T_e and n_e are computed for all 53 regions and averaged over central, top/bottom peripheral, and left/right peripheral regions. In spite of the noticeable discrepancies in reconstructed spectra shown in FIG. 5, they do not affect the line ratios and widths significantly, and their impacts on the inferred conditions are all within a few percent.

To summarize, the dominant source of discrepancies for the peripheral regions are i) systematic intensity lowering at the periphery due to spatial-resolution effects and ii) the periodic structure due to horizontal intensity gradients.

IV. PINHOLE SIZE VARIATION EFFECTS AND ITS CORRECTION

Each pinhole of the pinhole array has a slightly different size due to the pinhole size tolerance. This pinhole size variation could introduce bias into reconstructed images and spectra. In this section, we simulate the impact of the pinhole size-variation effects on the reconstructed images. We then introduce a correction and discuss how

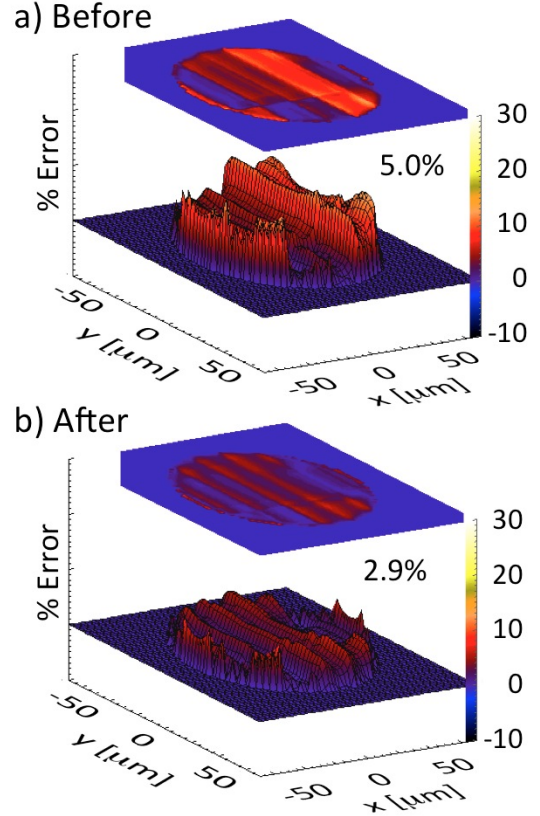


FIG. 7. (Color online) Percent error surface plots for the reconstructed He- β images (a) before and (b) after applying the pinhole size variation correction to the synthetic MMI data. Spatial-resolution effects are taken into account on the expected images.

well this correction removes the introduced bias from the reconstructed images and spectra.

First, we create synthetic MMI data with pinhole size-variation effects as discussed in Sec. II C. The pinhole size and its tolerance used in this synthetic study are $10 \pm 1 \mu\text{m}$, which are typical values for the pinhole array of our application. Both spectral resolution and spatial resolution are taken into account in the synthetic MMI data.

FIG. 7(a) shows the resultant percent-error surface plot for the reconstructed Ar He- β image. The spatial-resolution effect is applied on the expected image used in the percent-error calculation as discussed in Sec. III A. Compared to FIG. 3(c), the overall error increases from 1.4 to 5.0%. More importantly, it introduces a bias on the spatial shape. There is a larger error band ($\sim 10\%$) along the y direction. This must come from a single pinhole, which happens to have a significantly larger pinhole size than the nominal value.

The green lines in FIG. 8 are space-resolved spectra reconstructed from the synthetic MMI data with pinhole size variations for (a) a central region, (b) a bottom peripheral region, and (c) a left peripheral region.

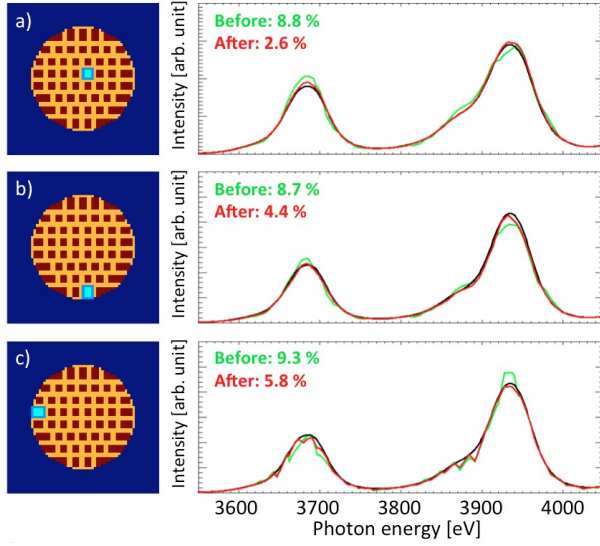


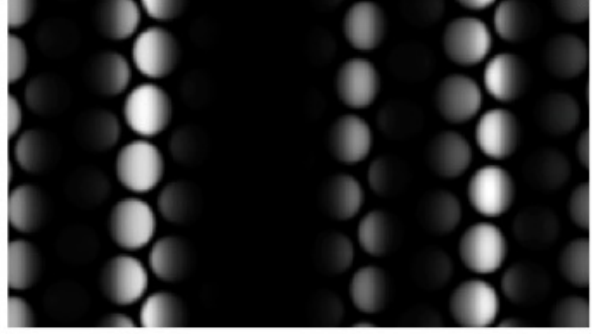
FIG. 8. (Color online) Space-resolved spectra over the He- β and Ly- β spectral range (blue) before and (red) after the pinhole size-variation correction for (a) a central region, (b) a bottom peripheral region, and (c) a left peripheral region. Black spectra are the expected spectra.

Compared to the reconstructed spectra without pinhole size-variation effects [i.e., the green lines in FIG. 5], the overall percent errors increase from (a) 0.2 to 8.8%, (b) 5.5 to 8.7%, and (c) 6.5 to 9.3%, respectively. For peripheral regions, one might think that the impact is not as large since the errors without pinhole size-variation effects are already showing $\sim 6\%$. However, percent errors without pinhole size-variation effects are systematic without changing the line ratios and widths [i.e., the green lines in FIG. 5], while percent errors due to the pinhole size-variation effects could affect the line ratios and the widths. Thus, from a diagnostics point of view, the errors due to the pinhole size-variation effects are more important than those due to the systematic intensity lowering and periodic structure discussed in Sec. III B.

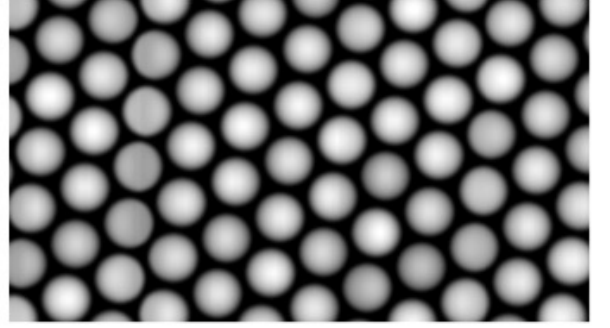
The introduced bias observed in this synthetic investigation is a concern for the actual MMI data analysis. For example, if one of the pinholes appearing at a line center happens to have a size larger than the vendor's tolerance, this could introduce significant spatial bias to the extracted images and spectra. Fortunately, the pinhole size variation can be estimated directly from the MMI data and corrected to first order.

Each pinhole size would affect each image of MMI data in two ways: 1) spatial resolution and 2) brightness. Of these two effects, the dominant effect is brightness variation from one image to another because brightness is proportional to the square of the diameter and thus 10% error in diameter results in 21% in brightness. FIG. 9 (a) shows the synthetic MMI data containing 10%-pinhole-size-variation effects used to reconstruct the images and spectra shown in FIG. 7 and 8. It is not clear which pinhole images are brighter or dimmer from the MMI data

a) Synthetic MMI with PH variation



b) After spectral content removed



c) Extracted brightness variation

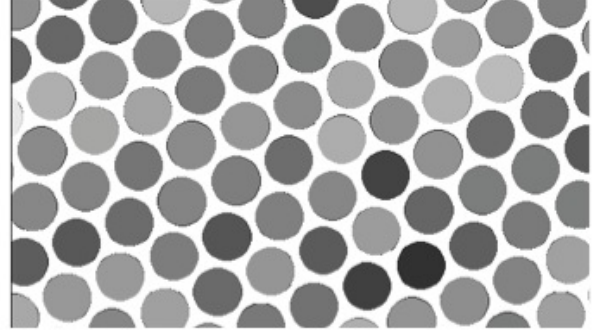


FIG. 9. (a) Synthetic MMI data with pinhole size-variation effects ($\Delta D/D = 0.1$). (b) Spectral contents are removed from (a). (c) Overall brightness of each pinhole is computed by integrating the intensity within each pinhole image and replacing the pixel values with this integration. We observed that the brightness is indeed slightly different for each pinhole image.

due to the horizontal spectral features on the MMI data. However, these spectral features can be roughly removed either by the Fourier-transform technique discussed by Izumi et al [8] or by simply dividing each row of the MMI data by the space-integrated spectrum.

FIG. 9(b) shows the synthetic MMI data with spectral features removed. It is now clearer which pinhole images are brighter or dimmer. Since we are interested in the overall brightness of each pinhole image, we integrate intensity values within each pinhole image and display each image according to its space-integrated intensity. FIG.

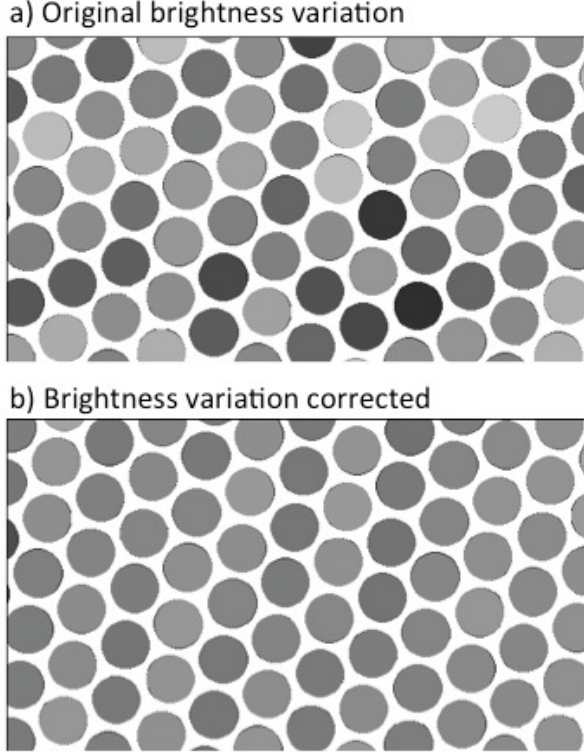


FIG. 10. (a) Original simulated brightness variations used to create FIG. 9(a). (b) Brightness variation after the correction is applied.

9(c) shows the resultant brightness-variation image. The brightness variation on the MMI data can be suppressed by dividing the MMI image [i.e., 9(a)] by this extracted brightness-variation image pixel-by-pixel.

Since FIG. 9(a) is the synthetic MMI data, the original brightness variation is known, and we can investigate how well this technique improves the results. FIG. 10(a) shows the original brightness variation used to create FIG. 9(a). FIG. 10(b) is the image computed by dividing FIG. 10(a) by the extracted brightness variation image [i.e., FIG. 9(c)]. It clearly shows that the correction suppresses the brightness variation significantly.

To quantitatively investigate the impact of the brightness-variation correction on the reconstructed images and spectra, the correction is applied to the synthetic MMI data [i.e., FIG. 9(a)]. Then, the percent-error surface plot for the He- β image is re-computed, and the space-resolved spectra are reconstructed for comparison.

FIG. 7 (b) shows the percent-error surface plot on He- β after the brightness-variation correction. The average error is reduced from 5.0 to 2.9%. More importantly, the spatial bias due to the pinhole size variation [i.e., large error band in FIG 7(a)] is significantly reduced.

The red curves in FIG. 8 show the space-resolved spectra reconstructed from the synthetic MMI data after the correction. The average percent error is reduced (a) from 8.8 to 2.6%, (b) from 8.7 to 4.4%, and (c) from 9.3 to

Intensity % error	Before	After
Central (32)	$5.3 \pm 0.3 \%$	$1.5 \pm 0.1 \%$
Top/bottom periphery (5)	$5.3 \pm 0.4 \%$	$3.1 \pm 0.3 \%$
Left/right periphery (16)	$7.8 \pm 1.2 \%$	$7.0 \pm 1.8 \%$

TABLE III. Average and standard deviation of the space-resolved spectra percent errors over the 32 central regions and over the 21 peripheral regions before and after the brightness-variation correction.

T_e % error	Before	After
Central (32)	$2.1 \pm 1.0\%$	$0.3 \pm 0.2\%$
Top/bottom periphery (5)	$2.4 \pm 1.3\%$	$1.0 \pm 1.1\%$
Left/right periphery (16)	$1.2 \pm 1.3\%$	$0.8 \pm 0.6\%$
n_e % error	Before	After
Central (32)	$2.8 \pm 2.0\%$	$2.0 \pm 1.0\%$
Top/bottom periphery (5)	$3.1 \pm 2.8\%$	$2.3 \pm 1.7\%$
Left/right periphery (16)	$5.7 \pm 4.5\%$	$1.7 \pm 2.4\%$

TABLE IV. The percent errors in T_e and n_e averaged over the central, top/bottom-periphery, and left/right-periphery regions, respectively. The errors decrease after the pinhole size-variation correction.

5.8%, respectively. One can visually confirm that the correction successfully removes the bias associated with the brightness variation and significantly improves the space-resolved spectra.

The same analysis is repeated for all the spectra, and the percent errors are summarized for each category in Table III. The average errors for the space-resolved spectra reconstructed for each category are lowered from 5.3 to 1.5% for central regions, 5.3 to 3.1% for top/bottom peripheral regions, and 7.8 to 7.0% for left/right peripheral regions. For the peripheral regions, the average error is still high because the main source of error is the systematic intensity lowering and the periodic oscillations. However, the bias introduced by the pinhole size-variation effects is successfully removed as shown in FIG. 8 (b) and (c). The conditions inferred from the corrected spectra are accurate with less than a few percent errors (Table IV).

V. DISCUSSION AND SUMMARY

While the MMI instrument is a powerful diagnostic tool to constrain spatial structure of inertial confinement fusion plasmas, the reliability of the reconstructed images and spectra has never been investigated. Due to the discrete nature of MMI data, the accuracy of the reconstructed images and spectra is somewhat limited. In this article, we synthetically investigated and quantified the accuracy of the images and spectra reconstructed from synthetic MMI data for the application of OMEGA direct-drive Ar-doped D_2 ICF implosion experiments.

The intensities of the reconstructed images are accurate with less than a few percent error as long as spatial effects are taken into account. The reconstructed space-resolved spectra are accurate for central regions of the core image. The intensities of the space-resolved spectra reconstructed for the peripheral regions are slightly but systematically lowered due to the MMI spatial-resolution effects on the spectra. This increases the percent error to 3 - 4%. We note that the exact effects on the periphery are more complicated because there is no discrete plasma boundary in real plasma. Especially, for ICF plasma, there is fuel-shell mixing due to hydrodynamic instabilities. These are very important aspects but beyond the scope of this article. For left/right peripheral regions, the reconstructed spectra inherits intrinsic horizontal intensity gradient, which results in periodic structure on the spectra. This increases the percent error to $\sim 7\%$. Fortunately, these systematic intensity-lowering and periodic structures do not change line ratios and widths significantly, and their impact on the plasma condition diagnostics is less than a few percent.

One potential source of bias in the reconstructed images and spectra is pinhole size-variation effects. The simulation shows this is small (i.e., $\sim 5\%$). However, we confirmed that it can introduce $\sim 10\%$ spatial bias in the reconstructed images and $\sim 10\%$ change in the line ratios in the spectra. Since some pinholes could have larger/smaller size beyond the vendor's specification, it

has to be somehow measured and corrected. We developed a technique to extract its dominant effect, brightness variation. The images and spectra reconstructed from the corrected MMI data successfully remove the bias introduced by the pinhole size variations. The conditions inferred from the corrected MMI data are accurate with less than a few percent errors.

These investigations provide a better understanding for the successful use of MMI diagnostics and the reliability and limitations of the reconstructed images and spectra for the OMEGA direct-drive ICF Ar-doped D_2 implosion experiments. MMI diagnostics are unique and constrains the object spatial information with unprecedented level of detail. However, the complexity of MMI data should not be underestimated. It is important to perform similar synthetic investigations for individual applications because the impact of each investigated issue, though similar, quantitatively differs per application.

ACKNOWLEDGEMENT

This work was supported by DOE/NLUF Grant No. DE-NA0000859 and DE-NA0002267, and LLNL. T. Nagayama thanks R. E. Falcon for his help in refining the manuscript. R. Florido thanks support from EUROfusion ToIFE project. Prepared in part by LLNL under Contract DE-AC52-07NA27344.

-
- [1] J. Nuckolls, L. Wood, A. Thiessen, and G. Zimmerman, *Nature* **239**, 139 (1972).
 - [2] J. D. Lindl, P. Amendt, R. L. Berger, S. G. Glendinning, S. H. Glenzer, S. W. Haan, R. L. Kauffman, O. L. Landen, and L. J. Suter, *Physics of Plasmas* **11**, 339 (2004).
 - [3] J. Lindl, O. Landen, J. Edwards, E. Moses, and N. Team, *Physics of Plasmas* **21**, 020501 (2014).
 - [4] D. S. Clark, M. M. Marinak, C. R. Weber, D. C. Eder, S. W. Haan, B. A. Hammel, D. E. Hinkel, O. S. Jones, J. L. Milovich, P. K. Patel, H. F. Robey, J. D. Salmonson, S. M. Sepke, and C. A. Thomas, *Physics of Plasmas* **22**, 022703 (2015).
 - [5] J. A. Koch, T. W. Barbee, N. Izumi, R. Tommasini, R. C. Mancini, L. A. Welser, and F. J. Marshall, *Rev. Sci. Instrum.* **76**, 073708 (2005).
 - [6] R. Tommasini, J. A. Koch, N. Izumi, L. A. Welser, R. C. Mancini, J. Delettrez, S. Regan, and V. Smalyuk, *Rev. Sci. Instrum.* **77**, 10E303 (2006).
 - [7] L. A. Welser, R. C. Mancini, J. A. Koch, S. Dalhed, R. W. Lee, I. E. Golovkin, F. Marshall, J. Delettrez, and L. Klein, *Rev. Sci. Instrum.* **74**, 1951 (2003).
 - [8] N. Izumi, T. W. Barbee, J. A. Koch, R. C. Mancini, and L. A. Welser, *Rev. Sci. Instrum.* **77**, 083504 (2006).
 - [9] T. Nagayama, R. C. Mancini, R. Florido, R. Tommasini, J. A. Koch, J. A. Delettrez, S. P. Regan, and V. A. Smalyuk, *J Appl Phys* **109**, 093303 (2011).
 - [10] T. Nagayama, R. C. Mancini, R. Florido, D. Mayes, R. Tommasini, J. A. Koch, J. A. Delettrez, S. P. Regan, and V. A. Smalyuk, *Physics of Plasmas* **21**, 050702 (2014).
 - [11] T. Nagayama, R. C. Mancini, R. Florido, R. Tommasini, J. A. Koch, J. A. Delettrez, S. P. Regan, V. A. Smalyuk, L. A. Welser-Sherrill, and I. E. Golovkin, *Rev. Sci. Instrum.* **79**, 10E921 (2008).
 - [12] T. Nagayama, R. C. Mancini, R. Florido, D. Mayes, R. Tommasini, J. A. Koch, J. A. Delettrez, S. P. Regan, and V. A. Smalyuk, *Physics of Plasmas* **19**, 082705 (2012).
 - [13] T. Nagayama, R. C. Mancini, D. Mayes, R. Tommasini, and R. Florido, Submitted to High Power Laser Science and Engineering (2015).
 - [14] M. F. Gu, *Can. J. Phys.* **86**, 675 (2008).
 - [15] R. Florido, R. Rodríguez, J. M. Gil, J. G. Rubiano, P. Martel, E. Mínguez, and R. C. Mancini, *Phys. Rev. E* **80**, 56402 (2009).
 - [16] J. C. Stewart and K. D. J. Pyatt, *The astrophysical Journal* **144**, 1203 (1966).
 - [17] R. C. Mancini, R. F. Joyce, and C. F. Hooper, Jr., *J. Phys. B: At. Mol. Phys.* **20**, 2975 (1987).
 - [18] R. C. Mancini, D. P. Kilcrease, L. A. Woltz, and C. F. Hooper, Jr., *Computer Physics Communications* **63**, 314 (1991).
 - [19] D. Mihalas, *Stellar Atmospheres*, Astronomy and Astrophysics Series (W. H. Freeman, 1978).